Structural Engineering and Mechanics, *Vol. 48, No. 4 (2013) 501-518*
DOI: http://dx.doi.org/10.12989/sem.2013.48.4.501

Exploring and calibrating local curvature effect of cortical bone for quantitative ultrasound (QUS)

Jiangang Chen[1,2], Zhongqing Su[*1], Li Cheng[1] and De-an Ta[3]

[1]*The Department of Mechanical Engineering, The Hong Kong Polytechnic University, Kowloon, Hong Kong*
[2]*The Ultrasound and Elasticity Imaging Laboratory, Department of Biomedical Engineering, Columbia University, New York, NY, USA*
[3]*The Department of Electronic Engineering, Fudan University, Shanghai, P.R. China*

(Received July 9, 2013, Revised October 14, 2013, Accepted October 26, 2013)

Abstract. Apart from thinning of cortical layers, the local bone curvature, varying along bone periphery, modulates ultrasound waves as well, which is however often underestimated or overlooked in clinical quantitative ultrasound (QUS). A dedicated three-dimensional finite element modelling technique for cortical bones was established, for quantitatively exploring and calibrating the effect of local curvature of cortical bone on ultrasound. Using a correlation-based mode extraction technique, high-velocity group (HVG) and low-velocity group (LVG) wave modes in a human radius were examined. Experimental verification using acrylic cylinders and in vitro testing using a porcine femur were accomplished. Results coherently unravelled the cortical curvature exerts evident influence on bone-guided ultrasound when RoC/λ<1 for HVG mode and RoC/λ<2 for LVG mode (RoC/λ: the ratio of local bone curvature radius to wavelength); the sensitivity of LVG mode to bone curvature is higher than HVG mode. It has also been demonstrated the local group velocity of an HVG or LVG mode at a particular skeletal site is equivalent to the velocity when propagating in a uniform cylinder having an outer radius identical to the radius of curvature at that site. This study provides a rule of thumb to compensate for the effect of bone curvature in QUS.

Keywords: local bone curvature; cortical bone; bone modelling; quantitative ultrasound (QUS); high-velocity group wave; low-velocity group wave; in vitro testing

1. Introduction

The axial transmission (AT) technique is a main modality of quantitative ultrasound (QUS) to clinically assess human long bones (e.g., tibia, distal radius or femur), owing to its superior capability of detecting not only deterioration in material properties (e.g., porosity) but also changes in geometrical features (e.g., cortical thickness). During measurement, a pair of transmitter and receiver (or a group of transmitters and receivers) with a short distance apart are placed in tandem on the same skeletal side along the bone axial direction (Bossy *et al*. 2004, Minonzio *et al*. 2010).The generated ultrasound waves are guided by the bone when their wavelengths are comparable to or in the same order of the cortical thickness (Muller *et al*. 2005, Tatarinov *et al*.

*Corresponding author, Professor, E-mail: MMSU@polyu.edu.hk

http://www.techno-press.org/?journal=sem&subpage=8 ISSN: 1225-4568 (Print), 1598-6217 (Online)

2005, Chen *et al*. 2010a,b, 2012a,b, 2013a,b, Xu *et al*. 2010, Song *et al.* 2011). By benchmarking baseline signals (i.e., signals captured from bones which are deemed healthy), the changes in wave propagation characteristics (e.g., velocity) can serve as symptomatic indicators for a diversity of bone diseases such as osteoporosis (the tibial cortex of osteoporotic patients is thinner than normal due to osteoporotic endosteal resorption) (Muller *et al*. 2005, Moilanen *et al*. 2006, Ta *et al*. 2009, Laugier and Haiat 2011).

To canvass bone-guided ultrasound, most studies hypothesised that the part of the bone covered by the transmitter-receiver pair in AT is locally flat, neglecting its curvature because the transmitter and receiver are a short distance apart. Lefebvre *et al*. (2002), based on an *in vitro* testing using the ox long bones, demonstrated that when the radius of a long bone is much larger than the ultrasound wavelength, the bone can be treated as a plate without evident errors in assessment. Ta *et al*. (2006, 2009) speculated that the effect of bone curvature is noticeable at relatively low frequencies only (less than megahertz). Le *et al*. (2010) used a flat layered model to mimic the bone and well explained the nature of ultrasound waves in long bones. Chen *et al*. (2012b, 2013a, b) also developed a flat layered model to study the coupling effect of soft tissues on wave propagation. In addition, most QUS techniques are manipulated by comparing the signals captured from a healthy bone and the signals from the bone under evaluation (the former is the alleged baseline signals). In both measurements, the healthy and current bones have the similar curvature at a specific skeletal site, and thus the bone curvature would not impair the evaluation results.

However, real bones are complex tubular structures with irregular cross-sections along bone axis, where the curvature varies along the bone circumference and for those bones of small radii in particular. Varying curvature endows the bone-guided ultrasound waves with somewhat subtle features and makes them behave differently from their counterparts in a plate-like structure. As reported recently (Ta *et al*. 2006, 2009, Moilanen *et al*. 2007a, b), bone-guided ultrasound may not be described accurately if a plate model used to mimic the bone, especially in those occasions where the bone has a thick wall, leading to erroneous assessment on cortical degradation. In contrast, using a tube model and explaining waves in bones using the theory of cylindrical waves (Moilanen *et al*. 2007b), the precision of QUS can be improved. These studies have stressed that in order to reach a precise and accurate evaluation using QUS, the bone curvature should ideally be taken into account and properly compensated for.

Not only is the medium curvature a concern in the clinical QUS, but it has been an intensive research subject in engineering community over years, as typified by guided-wave-based non-destructive evaluation for tubular structures (e.g., pipelines) (Cheeke *et al*. 1998, Lowe *et al*. 1998, Alleyne *et al*. 2001, Cawley *et al*. 2003, Leonard and Hinders 2003, Tua *et al*. 2005, Cau *et al*. 2006).The studies focusing on the curvature effect of tubular structures on wave propagation have reached a conclusion that the curvature effect can be ignored only when the wall thickness is far less than the cylinder diameter (Li and Rose 2006, Velichko and Wilcox 2009). However, it is not the case for the QUS-based evaluation for human bone because the diameter of a bone is comparable to the bone thickness at most skeletal sites. As a result, the effect of the bone curvature cannot be neglected if high-precision QUS is targeted.

To explore the propagation characteristics of ultrasound in bones has clear clinical significance and relevance. In this study, quantitative exploration and calibration of the effect of local curvature of cortical bone on the high-velocity group (HVG) and low-velocity group (LVG) wave modes (each comprising different cylindrical wave modes) in a human radius featuring different local curvatures was conducted, using a dedicated three-dimensional (3D) finite element (FE) modelling technique with experimental verification. An *in vitro* testing using a porcine femur was carried out

to supplement the understanding.

2. Experiments and methods

2.1 Guided waves in tubular structures: analytical explanation

First consider a regular thin-walled cylinder with its inner and outer radii being a and b along the axis, respectively. This cylinder possesses elastic and homogeneous properties (earlier studies (Moilanen *et al*. 2006, 2007a) have demonstrated that the human bones can be approximated using isotropic, elastic and homogeneous materials for the purpose of studying ultrasound wave propagation). The waves guided by such a cylinder can be defined using the theory of cylindrical waves, and determined by the *characteristic frequency equation*

$$\left|D_{ij}\right| = \left|D_{ij}(\omega, k, c_L, c_T, a, b)\right| = 0, \quad (i, j = 1, 2, \cdots, 6) \tag{1}$$

where k and ω are the wavenumber and circular frequency of the wave mode, respectively; c_L and c_T are the velocities of the longitudinal and transverse (shear) wave modes in the cylinder, respectively, subjected to material properties. Eq. (1), called *characteristic frequency equation*, correlates material properties (c_L and c_T), cylinder dimensions (a and b) with wave propagation characteristics (ω and k). The roots to Eq. (1) depict the dispersion attributes of various wave modes guided by the cylinder. Further, the group velocity of a particular wave mode can be given by

$$c_{group} = \frac{\partial \omega}{\partial k}, \tag{2}$$

namely the local slope of $\omega - k$ curves, which was rearranged in this study as

$$\frac{\partial \omega}{\partial k} = \frac{\partial \left|D_{ij}\right|}{\partial k} \Big/ \frac{\partial \left|D_{ij}\right|}{\partial \omega}. \tag{3}$$

Equation (3) tactically avoids the efforts in seeking respective expression of ω and k, while requests $\frac{d\left|D_{ij}\right|}{dk}$ and $\frac{d\left|D_{ij}\right|}{d\omega}$ only, and makes it possible to achieve the group velocity of a wave mode at different frequencies by calculating the derivatives of the characteristic matrix defined by Eq. (1). With such a process, the obtained dispersion curves (group velocity *vs.* frequency) for different cylindrical wave modes in an isotropic, elastic and homogeneous cylinder (10 mm in outer radius and 3 mm in wall thickness, with the material properties of a typical human cortical bone as detailed in Table 1 are exhibited in Fig. 1. As highlighted in the diagram, there are two groups of cylindrical wave modes, from 150 to 300 kHz (the frequency range of interest in this study): (i) the *high-velocity group* (HVG) wave modes (including $L(0, 2)$ and $F(1, 3)$); and (ii) the *low-velocity group* (LVG) wave modes (consisting of $F(1, 1)$, $F(1, 2)$ and $L(0, 1)$). The HVG and LVG in tubular structures are corresponding to the first-arriving-signal and the second-arriving-signal (or called second wave elsewhere) (Nicholson *et al*. 2002, Laugier and Haiat 2011, Chen *et al*. 2013), respectively. Particularly, the particles have predominately axisymmetric axial displacement in L series modes, while radial displacements in F-series modes. Both groups present less dispersion

Table 1 Material properties of the cortical bone and acrylic cylinder used in FE simulation and experimental verification

	Density [g/cm^3]	Modulus of elasticity [GPa]	Poisson's ratio
Cortical bone	1.85	16.46	0.373
Acrylic cylinder	1.19	4.24	0.39

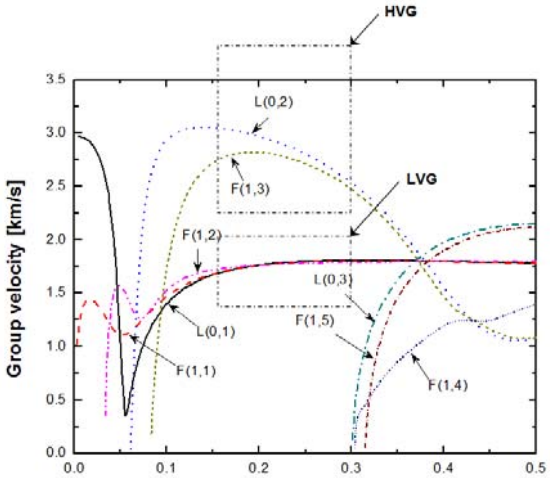

Fig. 1 Dispersion curves (group velocity vs. frequency) for different cylindrical wave modes in an isotropic, elastic and homogeneous cylinder (10 mm in outer radius and 3 mm in wall thickness, with the material properties of a typical human cortical bone in Table 1)

and slight fluctuation in their respective group velocities in from 150 to 300 kHz (such a frequency range is therefore called *less-dispersion region* hereinafter). In AT measurement (provided the diagnostic waves excited at a frequency falling in the less-dispersion region), the HVG modes arrives at the receiver first, followed with the LVG modes.

2.2 Modelling of guided waves

A 3D FE model for a typical human radius was created in ABAQUS®/CAE in conjunction with the use of a computed tomography (CT) imaging. The contour of the bone model is shown in Figs. 2(a) and (b), which was extracted from a CT image for a healthy adult radius (Moilanen *et al*. 2007a). The model had an axial length of 80 mm and an approximately uniform cortical thickness of 3 *mm*. The human radius was selected because it features a highly irregular profile with distinct curvatures along its periphery. Three-dimensional eight-node brick elements, with the material properties given in Table 1 for healthy adult cortical bone, were employed to define the model. An encastre boundary condition was applied. To guarantee the simulation precision, the maximum dimension of all the FE elements was less than 1 mm, leading to at least eight elements per wavelength of the LVG mode, the wave mode which has the smaller wavelength between two discussed wave groups at a given frequency in the less-dispersion region. Denser meshing was also examined, whereas to confirm that the current selection of eight elements per wavelength suffices to depict the propagation behaviours of both HVG and LVG modes accurately in the bone.

An AT measurement, using a pair of ultrasonic transducers (both having a diameter of 5 mm, one serving as the transmitter, and the other as the receiver, 45 mm apart) allocated in tandem and in contact with the surface of the bone model, was simulated. The transmitter was modelled using a piezoelectric transmitter model (Su and Ye 2005, Su *et al*. 2007). Uniform out-of-plane (perpendicular to the bone surface) displacement constraints were applied on the FE nodes on the outer surface of the piezoelectric element in the transmitter (i.e., at the interface in contact with the bone model), to emit diagnostic waves into the bone, to be consistent with the mechanism of an ultrasound transmitter used in the clinic. With this transmitter model, five-cycle *Hanning*-windowed sinusoidal tonebursts were activated at a central frequency of 200 kHz, falling in the less-dispersion region and also in the frequency range widely adopted in clinical QUS (Lee and Yoon 2004). The ultrasound waves in the bone model were captured using a piezoelectric receiver model (Su and Ye 2005, Su *et al*. 2007) which linked the deformations (strain, stress and displacement) in three orthogonal directions of the FE nodes on the outer surface of the piezoelectric element in the receiver to the magnitude of produced electrical signals.

The highly irregular profile of the selected radius along its periphery allows eight skeletal sites with significantly different local curvatures, SoI-1~SoI-8 (SoI: site of interest) as indicated in Fig. 2(c), at each of which AT measurement was simulated, respectively using the above modelling technique. Also indicated in Fig. 2(c) is the radius of local curvature, R, at each SoI, which was calculated in accordance with

$$\mathrm{R} = \sqrt{(x_1 - \alpha)^2 + (y_1 - \beta)^2}\ , \tag{4a}$$

Where (α, β) are the coordinates of the centre of the local curvature at an SoI, and

$$\alpha = \frac{\dfrac{x_1^{\,2} - x_2^{\,2} + y_1^{\,2} - y_2^2}{2(y_1 - y_2)} - \dfrac{x_1^{\,2} - x_3^{\,2} + y_1^{\,2} - y_3^2}{2(y_1 - y_3)}}{\left(\dfrac{x_1 - x_2}{y_1 - y_2} - \dfrac{x_1 - x_3}{y_1 - y_3}\right)}, \tag{4b}$$

$$\beta = \frac{x_1^{\,2} - x_2^{\,2} + y_1^{\,2} - y_2^2}{2(y_1 - y_2)} - \alpha \frac{x_1 - x_2}{y_1 - y_2}. \tag{4c}$$

In the above (x_1, y_1), (x_2, y_2) and (x_3, y_3) are three spatial points closely located on the bone periphery near a discussed SoI. The radii of local curvature at eight selected SoIs span widely from a minimum of 4.7 mm (SoI-5) to a maximum of 72.6 mm (SoI-6). A 3D model for the bone with a length of 80 mm was subsequently formed by protruding the cross-section profile shown in Fig. 2(c), as exhibited in Fig. 2(d). With the model, the simulation was carried out using ABAQUS/EXPLICIT®. The step of dynamic calculation was controlled to be less than the ratio of the minimum distance between two adjoining FE nodes to the highest group velocity of all involved wave modes (i.e., the HVG modes).

2.3 Experimental verification

Nine acrylic cylindrical phantoms, each having a uniform wall thickness of 2 mm and a length of 120 mm whereas different outer radius (from 8 to 32 mm, as enumerated in Table 2, were

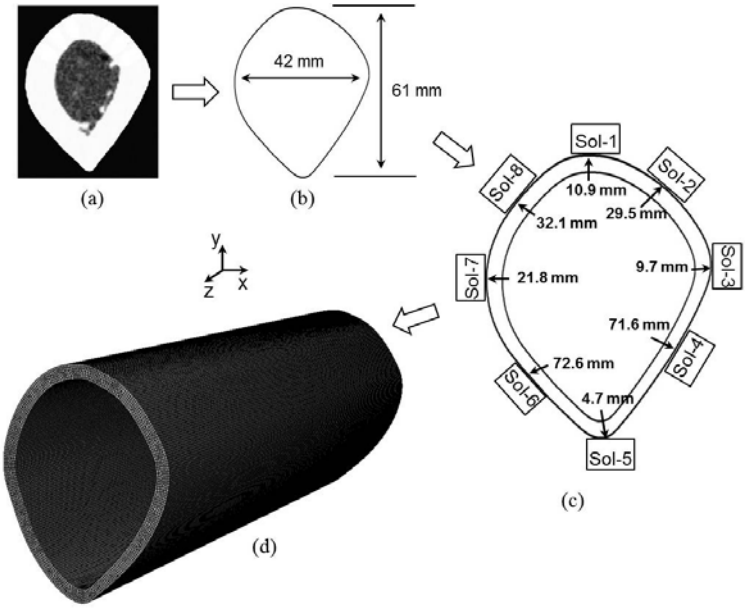

Fig. 2 Illustration for 3D modelling of human radius: (a) CT image of bone cross-section; (b) profile contour of bone cross-section; (c) profile showing eight selected SoIs; and (d) 3D model with an axial length of 80 mm by protruding the 2D cross-section

prepared for mimicking long bones of different local curvatures. The acrylic, a kind of prevailing bone-mimicking material, has been widely used to imitate cortical bones by virtue of its similarity to human bone in many material properties (e.g., density: $\rho_{acrylic}$ = 1.19 g/cm^3 vs. $\rho_{real\ bone} \approx$ 1.85 g/cm^3; modulus of elasticity: $E_{acrylic}$ = 4.24 GPa vs. $E_{real\ bone} \approx$ 2~20 GPa (Dong and Guo 2004); Poisson's ratio: $v_{acrylic}$ = 0.39 vs. $v_{real\ bone} \approx$ 0.373). Acrylic can easily be tailored to accommodate various bone geometries. Each phantom was supported on its two ends on an optical testing table. A pair of ultrasound transducers (IP0101GP, Valpey Fisher®, Hopkinton, MA, USA), serving as transmitter and receiver, respectively, was collocated in contact with the upper surface of each phantom via a wedge made of the same acrylic material (insert in Fig. 3). The wedge was specially trimmed to adapt to the curvature of each phantom, insuring adequate mechanical and acoustical coupling between transducers and phantoms, so as to minimise the loss of ultrasound energy during measurement. A total of nine such wedges were fabricated to accommodate nine phantoms, respectively. The transducer pair was instrumented with a signal generation/acquisition system (Chen *et al*. 2010a), as illustrated in Fig. 3. The diagnostic signal, five-cycle *Hanning*-windowed sine bursts at several candidate frequencies (from 150 to 300 kHz with an increment of 25 kHz), was generated using an arbitrary waveform generation unit (E1441, Agilent®, CA, USA), in which D/A conversion was conducted. The analog signals were amplified to 180 $V_{p\text{-}p}$ (peak-to-peak) with a linear amplifier (EPA-104, PiezoSys®, Jena, Deutschland) to drive the transmitter. Cylinder-guided waves were captured with a signal digitizer (E1438A, Agilent®, CA, USA) through the receiver at a sampling rate of 40 *MHz*. With the same configuration, a series of AT measurements was conducted, with different distances between transmitter and receiver, to provide measurement redundancy.

Table 2 Dimensions of acrylic cylinders used in experimental verification

Sample No.	Outer radius [mm]
1#	8
2#	9.5
3#	12
4#	15
5#	17
6#	20
7#	24
8#	28
9#	32

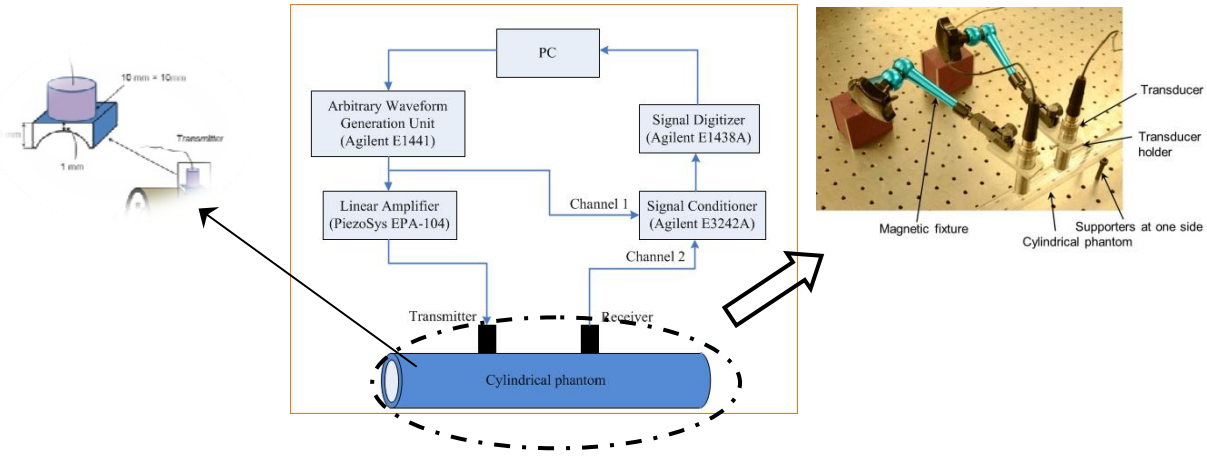

Fig. 3 Experimental set-up for AT measurement

2.4 In vitro testing using porcine femur

A porcine femur (a typical long bone) with a length of about 130 mm and a cortical thickness of approximately 3 mm was obtained from the local slaughterhouse, which was pre-processed by removing the coupled soft tissues and marrow. This deliberately selected femur, as seen in Fig. 4, features distinctly different local curvatures along its periphery. Exemplarily, two adjacent SoIs are indicated in the figure with the radii of local curvature being 44.3 mm (SoI-1) and 5.5 mm (SoI-2) (calculated using Eq. (4)), respectively. The diagnostic signal, the same as that used in preceding experimental validation, was excited at a sweep frequency from 150 to 300 kHz with an increment of 25 kHz. The bone-guided ultrasound waves were acquired at different SoIs of the femur with the abovementioned signal generation/acquisition system and measurement configuration.

2.5 Signal processing, results, discussion and calibration

Travelling at high velocities in bones (e.g., circa 2800 m/s for HVG and 1700 m/s for LVG modes at 200 kHz), the HVG and LVG modes, as well as other wave components such as their

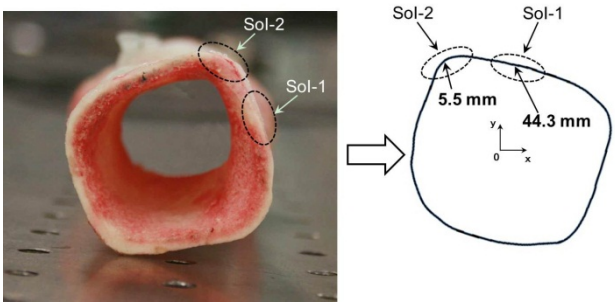

Fig. 4 A porcine femur with two example SoIs for in vitro testing

reflection from bone ends, may superimpose considerably with each other in the time domain, due to the short distance between transmitter and receiver in AT measurement. The difficulty in isolating the HVG or the LVG mode from other wave components poses a challenge on signal interpretation. To circumvent such a problem, a signal processing approach, *correlation-based mode extraction technique*, was developed.

The premise of the approach is that a captured time-domain signal $s(t)$ can be hypothesised to be the algebraic sum of a multitude of input signals (denoted by $\xi(t)$) which are delayed and attenuated to different extents (whereas less change in their waveforms). Such an assumption is based on the fact that (i) the transmitter and receiver in AT measurement are in a short distance apart (therefore less effect of absorption and nonlinearity of the medium); and (ii) the selected frequency falls in the less-dispersion region. Full discussion on the attenuation of ultrasound in QUS and the influence on waveform can be referred to elsewhere (Minonzio *et al*. 2011). Based on this, it has (Shi and Ihn 2001, Wang and Yuan 2009, Yu *et al*. 2011)

$$s(t)=\sum_{i=1}^{K} a_i h_i(t)=\sum_{i=1}^{K} a_i h_i\left(\frac{t-\tau_i}{s_i}\right), \qquad \left(i=1, 2, 3, \cdots K\right) \tag{5}$$

where $a_i h_i(t)$ represents the ith wave components included in $s(t)$ (K in total within the time period of interest), each having a unit magnitude of $|h_i(t)|$. a_i is an attenuation coefficient to rectify the magnitude of $|h_i(t)|$, subjected to the wave propagation distance. Note that $a_i h_i(t)$ is identical to $\xi(t)$ in waveform, provided wave dispersion is ignorable. τ_i is the arrival time of component $a_i h_i(t)$, while s_i a factor for quantifying the dispersion of waveform which was set as the unity in this study standing for ignorable wave dispersion.

For illustration, Fig. 5(a) shows an input diagnostic signal $\xi(t)$, five-cycle *Hanning*-windowed sinusoidal tonebursts at 200 kHz, which can be discretised with M sampling points during the acquisition (thus $\xi(t)$ retreats to $\xi(m)$, m = 1, 2, 3, …, M); Fig. 5(b) displays an accordingly captured signal $s(t)$, which can be discretised with N sampling points (similarly, $s(t)$ becomes $s(n)$, n = 1, 2, 3, …, N) (obviously $N > M$). Note that both the input and the captured signals are discretised using the same sampling rate (40 MHz in this example). In the approach, $s(n)$ is first truncated by shifting a window of the same length to that of $\xi(m)$ with a tiny step; at each step of the shifting, the fragment of $s(n)$ confined within the window, denoted by $x(m)$ (m = 1, 2, 3, …, M), is compared against $\xi(m)$ in terms of the similarity in between. Figure 5(b) illuminates schematically the four consecutive shifts of such a window applied to the captured signal. Upon each shift, the similarity between $x(m)$ and $\xi(m)$ is quantified in accordance with a correlation

coefficient, $\lambda_{x\xi}$, which is defined as (Li *et al*. 2006, Zhao *et al*. 2007, Yu *et al*. 2011)

$$\lambda_{x\xi} = \frac{M\sum_{m=1}^{M} x(m)\xi(m) - \sum_{m=1}^{M} x(m)\sum_{m=1}^{M} \xi(m)}{\sqrt{M\sum_{m=1}^{M} x(m)^2 - (\sum_{m=1}^{M} x(m))^2} \cdot \sqrt{M\sum_{m=1}^{M} \xi(m)^2 - (\sum_{m=1}^{M} \xi(m))^2}} \tag{6a}$$

or

$$\lambda_{x\xi} = \frac{C_{x\xi}}{\sigma_x \cdot \sigma_\xi} = \frac{\sum_{m=1}^{M} (x(m) - \mu_x)(\xi(m) - \mu_\xi)}{\sqrt{\sum_{m=1}^{M} (x(m) - \mu_x)^2} \cdot \sqrt{\sum_{m=1}^{M} (\xi(m) - \mu_\xi)^2}}, \tag{6b}$$

where $C_{x\xi}$, μ and σ are the covariance, mean and standard deviation of $x(m)$ and $\xi(m)$, respectively, distinguished by subscript for two signals. When $\xi(m)$ is very similar to the windowed fragment $x(m)$, the correlation coefficient defined by Eq. (6) approaches unity; the greater the similarity between the two signals the closer to unity is $\lambda_{x\xi}$. Upon completion of each shifting, $\lambda_{x\xi}$ is calculated; when $\lambda_{x\xi}$ reaches its extremum after a particular shift, it is deemed that the current time used for shifting the window is namely the arriving time of the ith wave component (i.e., τ_i in Eq. (5)). As $s(n)$ consists of a multitude of $\xi(m)$ with different τ_i, a series of extrema of $\lambda_{x\xi}$ can be achieved provided the window is shifted through full length of the captured signal. Via such a processing, different wave modes included in a captured signal can be isolated.

Once a particular wave mode is recognised and its τ_i is ascertained, this mode is then subtracted from $s(n)$, leading to a residual, $r_i(t)$, which, upon the ith subtraction, is

$$r_i(n) = r_{i-1}(n) - a_i h_i(n - \tau_i). \quad (i = 1, 2, 3, \cdots K) \tag{7}$$

In particular, $r_0(n)$ is the original signal $s(n)$. Such a processing constitutes the basic framework of the *correlation-based mode extraction technique* in this study. Appling the above mode isolation technique on the signal in Fig. 5(b) in which the HVG and the LVG modes partially overlapped in the time domain, Figs. 6(a) and (b) show the first two subtraction (i.e., $r_1(n)$ and $r_2(n)$) using Eq. (7), clearly standing out the HVG and the LVG modes, respectively. Further, Fig. 6(c) presents the residual signal upon subtraction of both isolated wave modes from the original signal, to observe that the residual signal is of insignificant magnitude, demonstrating the HVG and the LVG modes are dominant in the original signal.

Such a mode isolation approach shows advantages in certain aspects, compared with traditional mode separation approaches such as those based on the wavenumber-frequency or time-frequency analysis, including (i) the avoidance of using a dense sensor network (in a wavenumber-frequency analysis, a number of spatially distributed transducers are often compulsory for multi-point measurement (Sasso *et al*. 2006)), and (ii) the applicability to signals with highly superposed multi-wave modes (in a time-frequency analysis, the attempt to isolate severely overlapped modes is often vain if those modes are in the same frequency band). All the acquired ultrasound signals from simulation, experimental validation and *in vitro* testing were processed with the correlation-based mode extraction technique, to isolate the HVG and the LVG modes for subsequent signal interpretation.

3. Results and discussions

3.1 Simulation results vs. analytical results

To extend the discussion to a wider spectrum and allow the variation in excitation frequency, a hybrid factor involving both the bone curvature and the excitation frequency was introduced, defined as the ratio of the radius of local curvature (outer periphery of the bone) to the wavelength (denoted by RoC/λ hereinafter). With it, the group velocities of the HVG and the LVG modes against RoC/λ are plotted in Figs. 7(a) and (b), respectively. To compare with analytical results, displayed in Fig. 7 also include the group velocities of $L(0, 2)$ (a representative wave mode included in the HVG as elucidated previously) in Fig. 7(a), and $F(1, 1)$ (a typical mode in the LVG) in Fig. 7(b). These analytical results were obtained using Eqs. (1)-(3) from eight regular cylinders, each of which respectively had a radius the same as the radius of local curvature at eight SoIs of the bone model as shown in Fig. 2. A good agreement between the simulation and analytical results was achieved in Fig. 7, unveiling that a bone-guided wave mode (either the HVG or the LVG mode) locally adapts itself to the bone curvature, and its group velocity at a specific skeletal site is equivalent to the velocity when it propagates in a regular cylinder having a radius the same as the local curvature at that skeletal site. In the above, the theoretical values were calculated using software DISPERSE® which considered the bone as a geometrically regular tube, while the simulation results were obtained at eight SoIs of the irregular bone model. Such discrepancy results in slight difference between the analytical and the simulation results (but less than 10%).

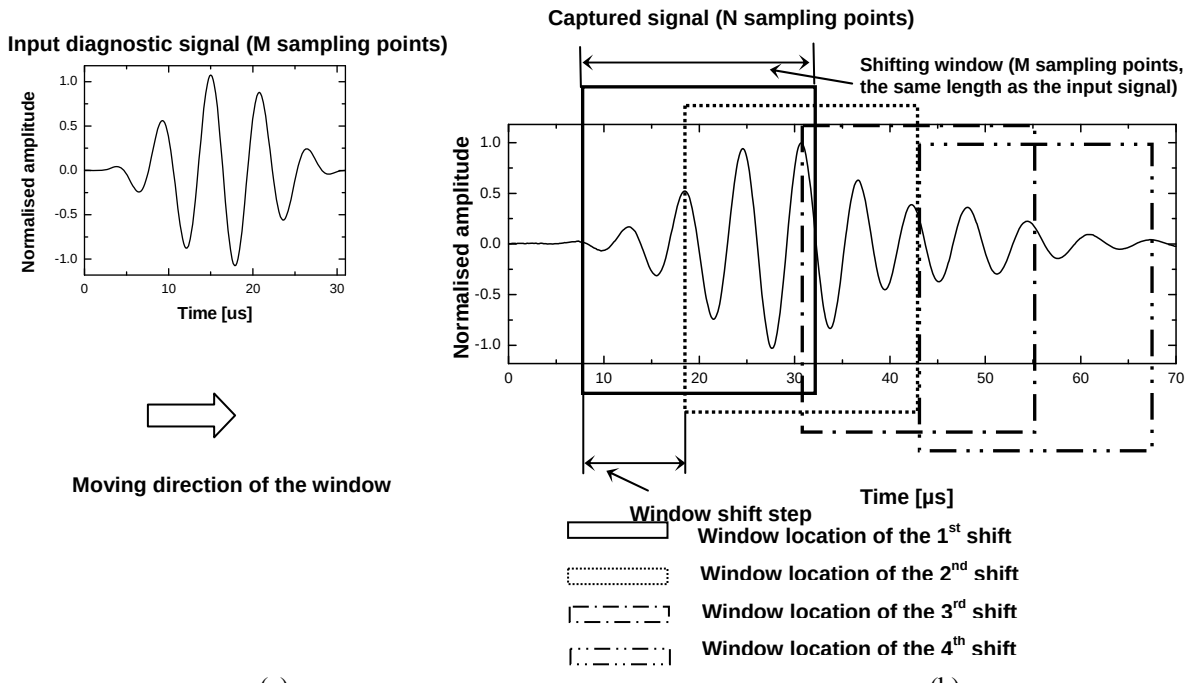

Fig. 5 Schematic illustration of the correlation-based mode extraction technique: (a) input diagnostic signal; and (b) captured signal, applied with four consecutive window shifting

As observed in Fig. 7, the group velocities of both the HVG and the LVG modes increase with increase in RoC/λ; and such a trend is particularly precipitous when RoC/λ is of small values (e.g., SoI-3 and SoI-5 where RoC/λ<1 for the HVG mode, and RoC/λ<2 for the LVG). The HVG mode propagates at an almost constant velocity when the radius of local bone curvature exceeds 10 mm (i.e., RoC/λ>1), which is therefore defined as the cut-off curvature radius for the HVG at current λ (indicated as the cut-off RoC/λ, in Fig. 7(a)); while for the LVG mode, such a threshold is circa 20 mm (i.e., RoC/λ>2, as highlighted in Fig. 7(b)). Figure 7 also recapitulates that the LVG mode is more susceptible to the effect of bone curvature than the HVG mode.

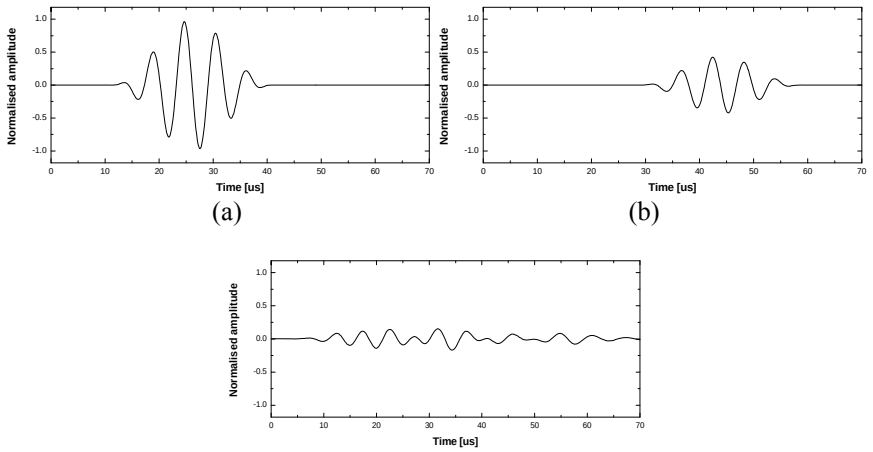

Fig. 6 Isolated (a) HVG and (b) LVG modes using the correlation-based mode extraction technique; and (c) residual signal after extraction of both isolated modes (magnitudes of signals are normalized with respect to that in (a))

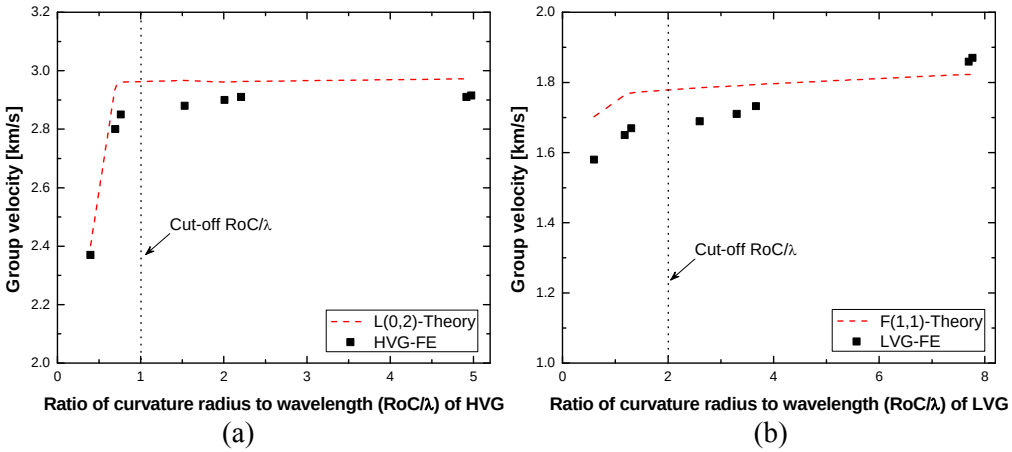

Fig. 7 Group velocities (from FE simulation and theory) of (a) HVG and (b) LVG modes against RoC/λ

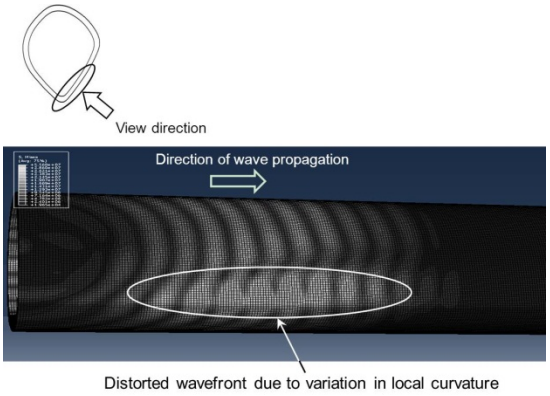

Fig. 8 Stress field of cortical bone-guided ultrasound at an example propagation instant in dynamic simulation, showing distortion of wavefronts at sites of different local curvatures (the lighter the greyscale the higher the stress is)

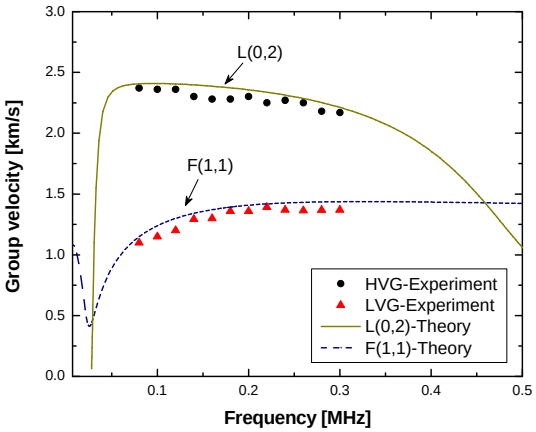

Fig. 9 Dispersion curves (experiment and theory) for HVG and LVG modes (using sample No. 4#)

To further comprehend the curvature effect on the HVG and the LVG propagation in cortical bones, the stress fields of both wave modes guided by the bone were calculated using the dynamic simulation, as displayed in Fig. 8 for an example instant. Severely distorted wavefronts are observed at the sites with a smaller radius of local curvature, manifested as the delayed dissemination of wavefronts in the bone. Such an intuitive observation tallies with the conclusions drawn in the above.

3.2 Experimental results vs. analytical results

As the representative results from experimental verification using the acrylic cylinders, Fig. 9 plots the dispersion curves for the HVG and the LVG modes (in sample No. 4# as an example), comparing with those theoretically derived using Eqs. (1)-(3) for $L(0, 2)$ and $F(1, 1)$, showing good match in between. Furthermore, Fig. 10 displays the group velocities of the HVG and the

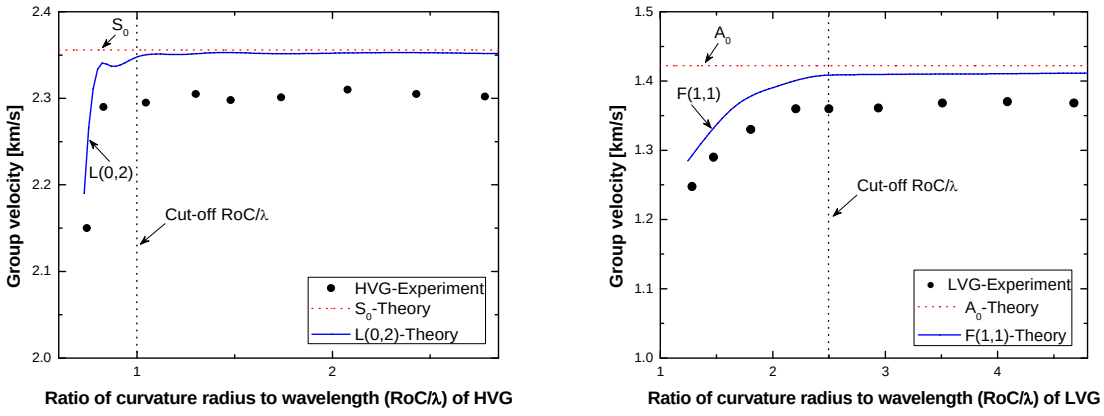

Fig. 10 Group velocities (experiment and theory) of (a) HVG and (b) LVG modes against RoC/λ

LVG modes against RoC/λ in nine acrylic cylinder phantoms listed in Table 2. To facilitate comparison with analytical results, the group velocities theoretically obtained for $L(0, 2)$ and $F(1, 1)$ are also included in Fig. 10. Conclusions can be drawn from Fig. 10: (i) the group velocities of both the HVG and the LVG modes increase as an increase in their respective RoC/λ; and (ii) the LVG mode has a higher sensitivity to the change in bone curvature than the HVG mode, manifested as a higher cut-off curvature radius (the cut-off RoC/λ for the LVG is about 2.5) which is twice that of the HVG. The above two conclusions corroborated well those drawn from simulation as detailed previously.

3.3 In vitro testing results

Based on *in vitro* testing results obtained from the porcine femur, the dispersion curves for the HVG and the LVG modes at two representative SoIs (marked in Fig. 4) are plotted in Fig. 11(a), to unravel that both wave modes behavef distinctly at different bone curvatures. Both propagate faster at SoI-1 (local curvature radius being 44.3 mm) than at SoI-2 (5.5 mm). Such a distinction can be better evidenced using the increase in the velocity with regard to that at SoI-2, as shown in Fig. 11(b), which highlights that difference in bone curvature can introduce a significant variation in the group velocity, and it is, for example, 10% for the HVG and 18% for the LVG at 200 kHz. Such an observation tallies with preceding conclusions in simulation and experimental validation that the LVG mode possesses higher sensitivity to bone curvature than the HVG mode. It is also noteworthy that, as seen in Fig. 11(b), the variation rate in the velocity due to changes in bone curvature decreases as an increase in excitation frequency of the diagnostic signal, stressing a prominent influence of the bone curvature at lower excitation frequency.

3.4 Discussion and compensation in QUS

As observed in Figs. 7 and 10, the bone curvature effect on propagation of the HVG and the LVG mode is prevailing when RoC/λ is of relatively small values (e.g., in the bones of small dimension) with RoC/λ<1 for the HVG and RoC/λ<2 for the LVG; in contrast, such an effect is not

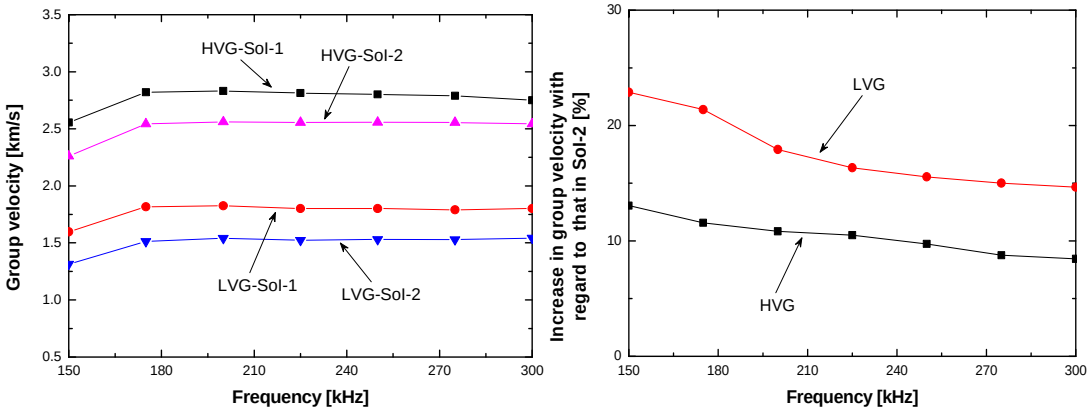

(a) (b)

Fig. 11 (a) Dispersion curves for HVG and LVG modes at two representative SoIs of the porcine femur shown in Fig. 4; and (b) increase in propagation velocity with regard to the velocity at SoI-2

evident provided RoC/λ is relatively large (e.g., in the bones of great dimensions) with RoC/λ>1 for the HVG and RoC/λ>2 for the LVG. All the results obtained in this study were based on either the theory of cylindrical waves or measurement from tubular structures. For further investigation, these results are compared with the group velocities of the fundamental symmetric and anti-symmetric plate wave modes (denoted by S_0 and A_0, respectively) in Fig. 10 (dotted lines). It is interesting to see that the greater the RoC/λ, the less the discrepancy between the HVG (represented by $L(0, 2)$) and S_0 it is, so is that between the LVG (represented by $F(1, 1)$) and A_0. This implies that a tubular bone structure can be hypothesised as a plate by ignoring its curvature only when the RoC/λ is relatively large (this can be achieved by using a higher excitation frequency and therefore a smaller wavelength), which is in line with the statement that the curvature is noticeable at low frequencies (Ta, Wang *et al*. 2009). Under such a circumstance, the ultrasound waves in bones can be depicted using the theory of plate waves (i.e., Lamb wave theory (Rose 1999)). This conclusion also corroborates the viewpoint from the engineering community that a tubular structure can be deemed as a periodic unwrapped plate when the wall thickness is far less than the cylinder diameter (Li and Rose 2006, Velichko and Wilcox 2009).

The above observations also accentuate that, subject to a hybrid factor involving both the bone curvature and the excitation frequency (RoC/λ), ignoring the bone curvature effect may incur compromised assessment or even erroneous results, if QUS is applied to bones of small dimension (e.g., phalanx or rib) where RoC/λ<1 for the HVG and RoC/λ<2 for the LVG); while such an effect is trivial and can be neglected, when QUS is used for evaluating bones of great dimension (e.g., tibia, radius) where RoC/λ>1 for the HVG and RoC/λ>2 for the LVG).

Between two discussed wave modes, the sensitivity of the LVG mode to the bone curvature is much higher than the HVG mode. This illustrates that, when QUS is used for assessing bones with a small RoC/λ, it is preferable to adopt the HVG mode, so as to minimise the influence of bone curvature on evaluation precision. If the LVG used, appropriate compensation for the bone curvature effect should be applied, based on the quantitative correlations obtained in this study (Figs. 7 and 10). It is relevant to note that the present study focused on the effect of local bone curvature, rather than the average cross-sectional curvature which also impacts on wave

propagation, as detailed elsewhere (Moilanenn *et al*. 2007b). In this study, the average bone radius used in FE was slightly smaller than those reported elsewhere (Moilanen *et al*. 2007b), with an intention to examine smaller bones featuring smaller local radii (i.e., from 4.7 to 72.6 mm). However such discrepancy would not downgrade the essence of the problem nor weaken applicability of the proposed method.

The bone curvature varies along the axis of cortical bone as well apart from the periphery, which introduces additional complicity to wave propagation. In practical QUS implementation, the transducer pair is often positioned at the skeletal sites where the local curvature is relatively constant along the bone axis, and the distance between the transmitter and receiver is short. These implement conditions can minimise the effect on wave propagation from the curvature variation along bone axis. In addition, propagation of ultrasound in cortical bone is compressively subject to a wide array of factors rather than bone curvature only such as bone thickness and material properties (Bossy *et al*. 2002, Nicholson *et al*. 2002, Laugier and Haiat 2011). The coupling effect arising from the surrounding soft tissues (skin, muscle, marrow, etc.) can also impact wave propagation (Ta *et al*. 2009, Chen *et al*. 2010, 2012a, b, 2013a, b). The current study is limited to exploring the local bone curvature effect only, while future studies on the effect arising from combined factors including cortical thickness, material properties, coupling effect of soft tissues and local bone curvature should be entailed, towards development of high-precision bone assessment techniques. On the other hand, validation using phantoms with inhomogeneous and anisotropic natures (e.g., Saw bone samples) warrants further investigation.

It is also noteworthy that, when compared with other factors that may alter propagation characteristics of ultrasound waves in cortical bones including mainly the inhomogeneity and anisotropy of the bone and tissues, the bone curvature impact much more significant influence on ultrasound waves. Earlier studies (Palmeri *et al*. 2005, Moilanen *et al*. 2006, Moilanen *et al*. 2007, Moilanen *et al*. 2007, Chen *et al*. 2010, Chen *et al*. 2013) have substantiated that the assumption of both bone and soft tissues being homogeneous and isotropic would not entail perceptible errors when canvassing ultrasound waves if QUS is manipulated in a relatively low frequency (in the order of hundred kilohertz).

4. Conclusions

The effect of the local curvature of cortical bone on propagation of the HVG (including cylindrical $L(0, 2)$ and $F(1, 3)$ modes) and the LVG (cylindrical $F(1, 1)$, $F(1, 2)$ and $L(0, 1)$ modes) was investigated quantitatively, through a dedicated 3D FE modelling and simulation technique, in conjunction with the use of CT imaging. Experimental verification using a series of acrylic cylinders with different curvatures and *in vitro* testing using a porcine femur were carried out. A good agreement among simulation, experimental verification and *in vitro* testing results was achieved, coherently unveiling that the bone curvature can modulate different bone-guided ultrasound modes to different extents, which should not be neglected when RoC/λ is less than 1 for the HVG and 2 for the LVG modes. In contrast, ultrasound waves can be explained using the theory of plate waves by ignoring the bone curvature effect, provided RoC/λ>1 for the HVG and RoC/λ>2 for the LVG modes. In addition, the LVG mode shows higher sensitivity to the variation in bone curvature than the HVG mode. Concerning a given bone to be assessed, this sensitivity decreases with an increase in the excitation frequency of the diagnostic waves. It was also demonstrated that the bone-guided waves adapt themselves to local bone curvature, behaving

similarly as their counterparts propagating in a regular cylinder having a radius the same as the local curvature at that skeletal site. This can be helpful in predicting the group velocity of a desired bone-guided wave mode in real cortical bones by taking into account the bone curvature effect. This study provides a rule of thumb to compensate for the effect of local bone curvature. In clinical implementation, the compensation can be achieved based on the calibration results rendered in this study and prior knowledge on anatomical dimensions which can be obtained with the assistant of imaging techniques such as CT or magnetic resonance imaging.

Acknowledgments

The work was supported by grants from the Hong Kong Polytechnic University (Project No.: A-PK22 and A-PE1F), the NSFC (Project Nos. 11174060, 11327405), the PhD Programs Foundation of the Ministry of Education of China (Project No. 20110071130004), the Science and technology support program of Shanghai (13441901900) and the New Century Excellent Talents of the Ministry of Education of China (No. NCET-10-0349).

References

Alleyne, D.N., Pavlakovic, B., Lowe, M.J.S. and Cawley, P. (2001), "Rapid long-range inspection of chemical plant pipework using guided waves", *Rev. Prog. Quant. Nondestr. Eval*., **20**, 180-187.

Bossy, E., Talmant, M., Defontaine, M., Patat, F. and Laugier, P. (2004), "Bidirectional axial transmission can improve accuracy and precision of ultrasonic velocity measurement in cortical bone: a validation on test materials", *IEEE Trans. Ultrason. Ferroelectr. Freq. Contral*, **51**(1), 71-79.

Bossy, E., Talmant, M. and Laugier, P. (2002), "Effect of bone cortical thickness on velocity measurements using ultrasonic axial transmission: a 2D simulation study", *J. Acoust. Soc. Am*., **112**(1), 297-307.

Cau, F., Fanni, A., Montisci, A., Testoni, P. and Usai, M. (2006), "A signal-processing tool for non-destructive testing of inaccessible pipes", *Eng. Appl. Artif. Intel*., **19**(7), 753-760.

Cawley, P., Lowe, M.J.S., Alleyne, D.N., Pavlakovic, B. and Wilcox, P. (2003), "Practical long range guided wave testing: applications to pipes and rail", *Mater. Eval*., **61**(1), 66-74.

Cheeke, J.D.N., Li, X. and Wang, Z. (1998), "Observation of flexural Lamb waves (A0 mode) on water-filled cylindrical shells", *J. Acoust. Soc. Am*., **104**(6), 3678-3680.

Chen, J., Cheng, L., Su, Z. and Qin, L. (2013a), "Modeling elastic waves in coupled media: estimate of soft tissue influence and application to quantitative ultrasound", *Ultrasonics*, **53**(2), 350-362.

Chen, J. and Su, Z. (2013b), "On ultrasound waves in bones with coupled soft tissues: a mechanism study and in vitro calibration", *Ultrasonics*. (in press)

Chen, J., Su, Z. and Cheng, L. (2010a), "Identification of corrosion damage in submerged structures using anti-symmetric Lamb wave mode", *Proceedings of the 5th European Workshop on Structural Health Monitoring*, Naples, Italy, Jul.

Chen, J., Su, Z. and Cheng, L. (2012b), "The medium coupling effect on propagation of guided waves in engineering structures and human bone phantoms", *Coupled Systems Mechanics*, **1**(4), 297-309.

Chen, J., Su, Z., Cheng, L. and Qin, L. (2010b), "Influence of soft tissues on ultrasonic Lamb waves in synthesised soft tissue-bone phantoms", *IFMBE Proceedings*, **31**(6), 1315-1318.

Dong, X.N. and Guo, X.E. (2004), "The dependence of transversely isotropic elasticity of human femoral cortical bone on porosity", *J. Biomech*., **37**(8), 1281-1287.

Laugier, P. and Haiat , G. (2011), *Bone Quantitative Ultrasound*, Springer, New York.

Le, L.H., Gu, Y.J., Li, Y.P. and Zhang, C. (2010), "Probing long bones with ultrasonic body waves", *Appl. Phys. Lett*., **96**(11), 114102.

Lee, K.I. and Yoon, S.W. (2004), "Feasibility of bone assessment with leaky Lamb waves in bone phantoms and a bovine tibia", *J. Acoust. Soc. Am*., **115**(6), 3210-3217.

Lefebvre, F., Deblock, Y., Campistron, P., Ahite, D. and Fabre, J.J. (2002), "Development of a new ultrasonic technique for bone and biomaterials in vitro characterization", *J. Biomed. Mater. Res*., **63**(4), 441-446.

Leonard, K.R. and Hinders, M.K. (2003), "Guided wave helical ultrasonic tomography of pipes", *J. Acoust. Soc. Am.*, **114**(2), 767-774.

Li, F.C., Su, Z.Q., Ye, L. and Meng, G. (2006), "A correlation filtering-based matching pursuit (CF-MP) for damage identification using Lamb waves", *Smart Mater. Struct*., **15**(6), 1585-1594.

Li, J. and Rose, J.L. (2006), "Natural beam focusing of non-axisymmetric guided waves in large-diameter pipes", *Ultrasonics*, **44**(1), 35-45.

Lowe, M.J.S., Alleyne, D.N. and Cawley, P. (1998), "Defect detection in pipes using guided waves", *Ultrasonics*, **36**(1-5), 147-154.

Minonzio, J.G., Foiret, J., Talmant, M. and Laugier, P. (2011), "Impact of attenuation on guided mode wavenumber measurement in axial transmission on bone mimicking plates", *J. Acoust. Soc. Am*., **130**(6), 3574-3582.

Minonzio, J.G., Talmant, M. and Laugier, P. (2010), "Guided wave phase velocity measurement using multi-emitter and multi-receiver arrays in the axial transmission configuration", *J. Acoust. Soc. Am*., **127**(5), 2913-2919.

Moilanen, P., Nicholson, P.H.F., Kilappa, V., Cheng, S. and Timonen, J. (2006), "Measuring guided waves in long bones: Modeling and experiments in free and immersed plates", *Ultrasound. Med. Biol*., **32**(5), 709-719.

Moilanen, P., Nicholson, P.H.F., Kilappa, V., Cheng, S.L. and Timonen, J. (2007a), "Assessment of the cortical bone thickness using ultrasonic guided waves: Modelling and in vitro study", *Ultrasound. Med. Biol*., **33**(2), 254-262.

Moilanen, P., Talmant, M., Nicholson, P.H.F., Cheng, S.L., Timonen, J. and Laugier, P. (2007b), "Ultrasonically determined thickness of long cortical bones: Three-dimensional simulations of in vitro experiments", *J. Acoust. Soc. Am*., **122**(4), 2439-2445.

Muller, M., Moilanen, P., Bossy, E., Nicholson, P., Kilappa, V., Timonen, J., Talmant, M., Cheng, S. and Laugier, P. (2005), "Comparison of three ultrasonic axial transmission methods for bone assessment", *Ultrasound. Med. Biol*., **31**(5), 633-642.

Nicholson, P.H.F., Moilanen, P., Karkkainen, T., Timonen, J. and Cheng, S. (2002), "Guided ultrasonic waves in long bones: Modelling, experiment and in vivo application", *Physiol. Meas*., **23**(4), 755-768.

Palmeri, M.L., Sharma, A.C., Bouchard, R.R., Nightingale, R.W. and Nightingale, K.R. (2005), "A finite-element method model of soft tissue response to impulsive acoustic radiation force", *IEEE Trans. Ultrason. Ferroelectr. Freq. Contral*, **52**(10), 1699-1712.

Rose, J.L. (1999), *Ultrasonic Waves in Solid Media*, Cambridge University Press, Cambridge, MA.

Sasso, M., Talmant, M., Haiat, G., Laugier, P. and Naili, S. (2006), "Development of a multi-dimensional SVD based technique for multi-receivers ultrasound used in bone status characterization", Fourth IEEE Workshop on Sensor Array and Multichannel Processing.

Shi, L.H. and Ihn, J.B. (2001), "Identification of time-domain refletometry measurement results by wavelet modeling", *The 3rd International Workshoip on Strucctural Health Monitoring*, Stanford.

Song, X., Ta, D. and Wang, W. (2011), "Analysis of superimposed ultrasonic guided waves in long bones by the joint approximate diagonalization of eigen-matrices algorithm", *Ultrasound. Med. Biol*., **37**(10), 1704-1713.

Su, Z., Yang, C., Pan, N., Ye, L. and Zhou, L.-M. (2007), "Assessment of delamination in composite beams using shear horizontal (SH) wave mode", *Compos. Sci. Technol*., **67**(2), 244-251.

Su, Z. and Ye, L. (2005), "A fast damage locating approach using digital damage fingerprints extracted from Lamb wave signals", *Smart Mater. Struct*., **14**(5), 1047.

Ta, D.A., Huang, K., Wang, W.Q., Wang, Y.Y. and Le, L.H. (2006), "Identification and analysis of multimode guided waves in tibia cortical bone", *Ultrasonics*, **44**(1), e279-e284.

Ta, D.A., Wang, W.Q., Wang, Y.Y., Le, L.H. and Zhou, Y.Q. (2009), "Measurement of the dispersion and attenuation of cylindrical ultrasonic guided waves in long bone", *Ultrasound. Med. Biol*., **35**(4), 641-652.

Talmant, M., Su, Z., Cheng, L. and Laugier, P. (2012a), "Measurement of guided mode wavenumbers in soft tissue-bone mimicking phantoms using ultrasonic axial transmission", *Phys. Med. Biol*., **57**(10), 3025-3037.

Tatarinov, A., Sarvazyan, N. and Sarvazyan, A. (2005), "Use of multiple acoustic wave modes for assessment of long bones: Model study", *Ultrasonics*, **43**(8), 672-680.

Tua, P.S., Quek, S.T. and Wang, Q. (2005), "Detection of cracks in cylindrical pipes and plates using piezo-actuated Lamb waves", *Smart Mater. Struct*., **14**(6), 1325-1342.

Velichko, A. and Wilcox, P.D. (2009), "Excitation and scattering of guided waves: relationships between solutions for plates and pipes", *J. Acoust. Soc. Am*., **125**(6), 3623-3631.

Wang, Q. and Yuan, S. (2009), "Wave rebuilding method for the active Lamb wave based structural damage imaging", *Chinese Journal of Astronautics*, **30**(3), 5.

Xu, K.L., Ta, D.A. and Wang, W.Q. (2010), "Multiridge-based analysis for separating individual modes from multimodal guided wave signals in long bones", *IEEE Trans. Ultrason. Ferroelectr. Freq. Contral*, **57**(11), 2480-2490.

Yu, L., Cheng, L. and Su, Z. (2011), "Correlative sensor array and its applications to identification of damage in plate-like structures", *Structural Control and Health Monitoring*, **19**(8), 650-671.

Zhao, X., Gao, H., Zhang, G., Ayhan, B., Yan, F., Kwan, C. and Rose, J.L. (2007), "Active health monitoring of an aircraft wing with embedded piezoelectric sensor/actuator network: I. Defect detection, localization and growth monitoring", *Smart Mater. Struct*., **16**(4), 1208-1217.